Pump and ionizing-probe dynamics in a simultaneous treatment of electronic and nuclear motion in LiH

Roger Y. Bello [1,2,*] Robert R. Lucchese [2] and C. William McCurdy[1,2]

[1]*Department of Chemistry, University of California, Davis, California 95616, USA*
[2]*Chemical Sciences Division, Lawrence Berkeley National Laboratory, Berkeley, California 94720, USA*

The dissociative single ionization of the LiH molecule using a two-color UV-UV pump-probe scheme is simulated in *ab initio* calculations demonstrating how the dynamics initiated on intermediate Rydberg states of diatomic molecules can be imaged by such experiments. The theoretical treatment combines nuclear motion with highly correlated descriptions of electronic continua and bound electronic states. Nuclear dynamics on Rydberg states are only weakly reflected by changes in photoelectron energies ejected by time-delayed ionizing pulses if the Rydberg potential curves parallel those of the ion states being produced. However, coincidence measurements guided by knowledge of the photoionization amplitudes as a function of internuclear distance can still reveal intermediate-state dynamics in pump-probe experiments.

I. INTRODUCTION

Pump-probe spectroscopy, with attosecond or femtosecond pulses, has evolved into a powerful tool to study and control nuclear and electronic dynamics in molecules. The description of such experiments poses a challenge to theoretical methods, in particular when one or both pulses can ionize the molecule. Molecular photoionization is sensitive to the effects of electron correlation not only in the initial and final bound electronic states but also in the ionization process itself. Electron correlation in the initial and ionic states changes with molecular geometry, and so does the coupling between ionization channels that leads to different ionic states that can energetically open or close with the motion of the nuclei.

Although different methods have been developed over the years that are capable of treating both electron correlation and interchannel coupling [1–14], fewer methodologies exist that simultaneously include nuclear dynamics. Fully correlated theoretical treatments of photoionization including the nuclear degrees of freedom have been mainly applied to the H_2 molecule [15–21]. There are a number of studies including nuclear dynamics in larger systems; however, the treatment of the continuum in them was largely uncorrelated [22–27]. In this context, we recently developed a method allowing fully correlated calculations including the nuclear degrees of freedom in diatomic molecules, beyond H_2.

In this approach, we make use of the multichannel Schwinger variational method [1,6–9,28] to describe the electronic continua, while standard quantum chemistry methods are used to extract potential-energy curves and dipole couplings between neutral states of the molecule. Then, the time-dependent wave function is expanded in a complete set of Born-Oppenheimer product basis functions of electronic

and nuclear vibrational states. The Schwinger variational method we apply here is based on a numerical representation of the scattering states, using a close-coupling expansion between ionic states that are described by highly correlated multireference configuration-interaction wave functions.

We recently applied this methodology [29] to investigate how a correlated treatment of the ionization problem describes the dynamics of the LiH molecule in pump and probe processes that populate and then dissociatively ionize the intermediate $A\,^1\Sigma^+$ first excited state of the molecule, as shown in Fig. 1(d). Levine, Remacle, and coworkers pioneered studies of coupled electronic and nuclear dynamics in this system [30–34] focusing on nonadiabatic coupling between bound states of LiH that can be excited by an optical pulse. Those studies raised the question on which we focus here, namely, how those dynamics are revealed in the time-resolved photoelectron angular distributions and energy spectra.

Our earlier study [29] found that, indeed, the changing character, from covalent to ionic, of the $A\,^1\Sigma^+$ state is visible in the photoelectron energies and angular distributions as well as in the kinetic energies of the dissociating Li^+ and H fragments. However, in the case of the $A\,^1\Sigma^+$ state the nuclear dynamics on the intermediate state and the changing character of the electronic state are probed differently at different geometries by the probe pulse because the photoionization amplitudes change rapidly with internuclear distance.

In short, the ionizing probe pulse does provide a picture of the intermediate-state dynamics, but through the "lens" of the photoionization process that changes with geometry due largely to changes in electron correlation. The knowledge of the geometry dependence of the action of the ionizing probe pulse allows full interpretation of that picture.

In this study, we apply the same theoretical approach to the description of the resonant two-color pump-probe ionization through $^1\Pi$ Rydberg excited states of the LiH molecule. In contrast to the $A\,^1\Sigma^+$ state, these Rydberg states present relatively shallow wells [35–39], as seen in Fig. 1, containing

*Present address: Departamento de Química Física Aplicada, Módulo 14, Universidad Autónoma de Madrid, 28049 Madrid, Spain.
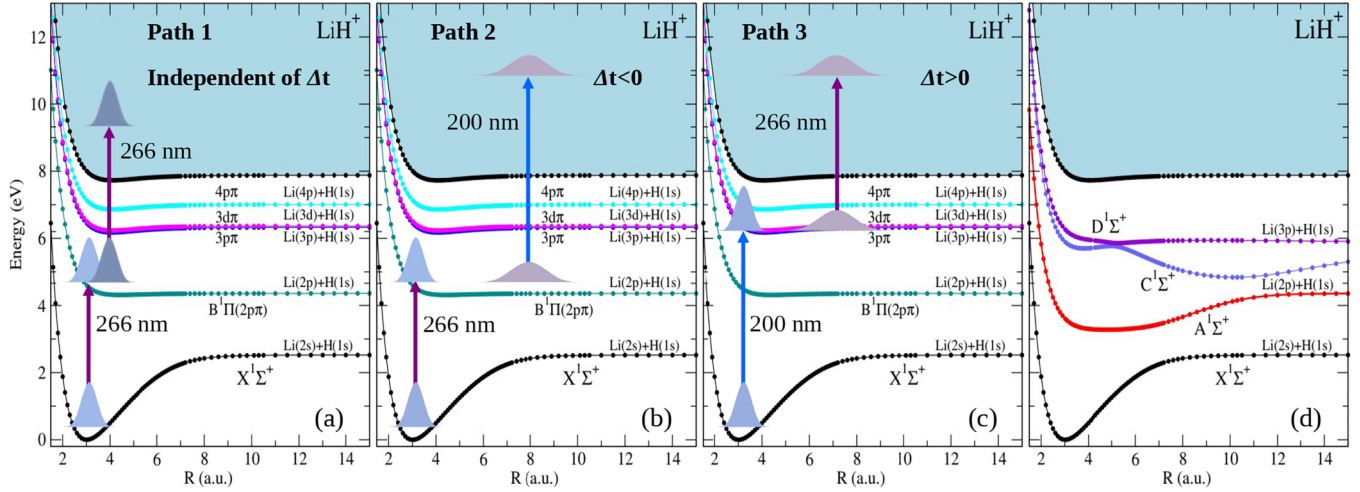
FIG. 1. Potential-energy curves for the four lowest $^1\Pi$ states of LiH and the $X^1\Sigma^+$ ground state. (a)–(c) The three paths to the ionization continuum are shown schematically for 5-fs pulses at 266 and 200 nm (bandwidth FWHM $\approx$1.24 eV). In these three panels the appropriate time delay Δt is indicated. (d) Potential curves for the ground state and three lowest $^1\Sigma^+$ excited states of LiH.

only a few bound vibrational states. Thus, resonant excitation occurs mainly through vibrational dissociative states. The higher photon energies required to pump these states open up multiple excitation and ionization pathways, leading to the same final states of the dissociating fragments. In this case the correlated treatment of photoionization reveals a simpler dependence of the probe on geometry. That simpler dependence allows an analysis of the angular and energy distribution of the photoproducts to unravel the multiple excitation and ionization paths leading to the same final states. However, for the Rydberg intermediate states we study here, it is the coincidence measurement of the photoelectron and the kinetic-energy release of the dissociating Li$^+$ and H fragments that provide the key to observing the dynamics on the states populated by the pump and probe pulses.

The outline of this paper is as follows. In Sec. II we briefly describe the theoretical framework, focusing on the Born-Oppenheimer expansion of the full wave function, including both ionization and dissociation continua, and also provide some computational details. In Sec. III we discuss the different pump-probe ionization pathways and the signatures they leave as a function of delay in the photoelectron energies and nuclear kinetic-energy release. In Sec. IV we summarize our findings and the possible applications of this methodology to more complex systems.

II. THEORETICAL FRAMEWORK

A. Born-Oppenheimer expansion of the wave function for nuclear and electronic dynamics

Our theoretical approach was described in detail earlier [29], so here we provide only a brief description of the main ideas. Atomic units are used throughout the following unless otherwise stated. We solve the time-dependent Schrödinger equation:

$$\left[\mathcal{H}(\mathbf{r}, R, t) - i\frac{\partial}{\partial t} \right] \Psi(\mathbf{r}, R, t) = 0, \tag{1}$$

where $\mathbf{r}$ represents all the spin and position coordinates of the electrons, R denotes the internuclear distance, and $\mathcal{H}(\mathbf{r}, R, t)$ is the complete Hamiltonian operator. The operator $\mathcal{H}(\mathbf{r}, R, t)$ can be formally written as

$$\mathcal{H}(\mathbf{r}, R, t) = \mathcal{H}_0(\mathbf{r}, R) + V(\mathbf{r}, t), \tag{2}$$

where $\mathcal{H}_0(\mathbf{r}, R)$ is the field-free Hamiltonian and $V(\mathbf{r}, t)$ is the laser-molecule interaction, here used in its velocity form. The field-free Hamiltonian $\mathcal{H}_0(\mathbf{r}, R)$ can be partitioned as the sum of the Born-Oppenheimer electronic Hamiltonian $H_0(\mathbf{r}; R)$ and the nuclear kinetic-energy operator,

$$\mathcal{H}_0(\mathbf{r}, R) = \hat{T}_N + H_0(\mathbf{r}; R). \tag{3}$$

The time-dependent wave function in Eq. (1) is expanded in a basis set of fully correlated adiabatic states similar to those of Refs. [15–19], with the explicit inclusion of the ionization continuum states [29]

$$\Psi(\mathbf{r}, R, t) = \sum_b \sum_{v_b} C_{bv_b}(t)\psi_b(\mathbf{r}; R)\chi_{v_b}(R)e^{-iE_{bv_b}t}$$

$$+ \sum_{\alpha l_\alpha m_\alpha} \int d\varepsilon_\alpha \sum_{v_\alpha} C_{\alpha v_\alpha}^{l_\alpha m_\alpha \varepsilon_\alpha}(t)$$

$$\times \psi_{\alpha l_\alpha m_\alpha}^{\varepsilon_\alpha(-)}(\mathbf{r}; R)\chi_{v_\alpha}(R)e^{-i(E_{\alpha v_\alpha} + \varepsilon_\alpha)t}. \tag{4}$$

In Eq. (4) $\psi_b(\mathbf{r}; R)$ are the bound states of the neutral molecule, and $\psi_{\alpha l_\alpha m_\alpha}^{\varepsilon_\alpha(-)}(\mathbf{r}; R)$ are the electron-ion scattering states that are the final continuum states of the photoionization process, labeled by asymptotic photoelectron energy and angular momentum (ε_α, l_α, and m_α) because they depend on the energy and direction of the photoelectron in each ionization channel. All the electronic states in Eq. (4) are defined as the eigenfunctions of the Born-Oppenheimer electronic Hamiltonian:

$$H_0(\mathbf{r}; R)\psi_b(\mathbf{r}; R) = E_b(R)\psi_b(\mathbf{r}; R),$$

$$H_0(\mathbf{r}; R)\psi_{\alpha l_\alpha m_\alpha}^{\varepsilon_\alpha(-)}(\mathbf{r}; R) = (E_\alpha(R) + \varepsilon_\alpha)\psi_{\alpha l_\alpha m_\alpha}^{\varepsilon_\alpha(-)}(\mathbf{r}; R). \tag{5}$$

The electronic continuum states are, in turn, represented in a close-coupling expansion using the multichannel Schwinger variational method [1,6–9,28] and labeled additionally by the channel α,

$$\psi_{\alpha l_\alpha m_\alpha}^{\varepsilon_\alpha(-)}(\mathbf{r};R) = \sum_{\beta l_\beta m_\beta} \mathcal{A}\Phi_\beta(\mathbf{r}';R)\phi_{\beta l_\beta m_\beta}^{\alpha l_\alpha m_\alpha(-)}(\mathbf{r}_N;R). \quad (6)$$

In the close-coupling expansion $\Phi_\beta(\mathbf{r}';R)$ denotes the eigenstates of the ion labeled by the index β, $\mathbf{r}'$ represents the $N-1$ electronic space and spin coordinates, $\mathcal{A}$ is the antisymmetrizer, and $\mathbf{r}_N$ denotes the space and spin coordinates of the electrons in the N-electron system, with the scattering functions $\phi_{\beta l_\beta m_\beta}^{\alpha l_\alpha m_\alpha(-)}(\mathbf{r}_N;R)$ satisfying Coulomb boundary conditions.

The Born-Oppenheimer vibrational states, bound or dissociative, $\chi_{v_b}(R)$ or $\chi_{v_\alpha}(R)$ in Eq. (4), defined on each of the potential-energy curves of the neutral and ionic electronic states of the molecule, satisfy

$$[\hat{T}_N + E_x(R)]\chi_{v_x}(R) = E_{xv_x}\chi_{v_x}(R), \quad (7)$$

where x denotes either the neutral electronically bound states b or the electronically bound states α of the ion and the potential-energy curves (PECs) $E_x(R)$ are the energies of the Born-Oppenheimer states appearing in Eq. (5). While calculating the dissociative states is, in general, a multichannel problem, where all PECs have to be included in the close-coupling expansion, we note that in the model used here we have included no nonadiabatic coupling between the states because there are no avoided crossings, and thus, such couplings are expected to be very weak. Thus, the problem can be reduced to calculating the dissociative states of each PEC individually.

The resulting representation of the time-dependent Schrödinger equation as a large set of coupled equations was described in Ref. [29]. The large number of those coupled equations arises from the quadratures of the nuclear dissociative continuum of every bound state included in the calculation and, most importantly, of the combined photoelectron continuum and dissociative vibrational continuum of the ion states in the double integral in Eq. (4).

B. Computational details

The PECs and dipole couplings between neutral states relevant to this study were computed using the multireference configuration-interaction (MRCI) capability of MOLPRO [40,41], with single and double excitations from an active space including eight σ and four π orbitals. These orbitals were optimized using a state-averaged complete-active-space (CAS) self-consistent-field calculation, with four $^1\Sigma^+$ and four $^1\Pi$ states included in the state average. The one-electron basis set was an augmented correlation-consistent polarized valence triple zeta (aug-cc-pVTZ) basis set augmented by four s, four p, and four d Rydberg diffuse functions [42] centered on the Li atom. MOLPRO performs contracted MRCI calculations, and these employed 200 608 contracted configuration-state functions (CSFs) in $^1\Sigma^+$ symmetry and 285 076 contracted CSFs in $^1\Pi$ symmetry. The resulting PECs are shown in Fig. 1 and present excellent agreement with earlier calculations [35–39].

The PECs discussed above were used in B-spline calculations of the bound and discretized continuum (dissociative) vibrational wave functions χ_{v_x}, which were restricted to zero rotational angular momentum. The vibrational wave functions were expanded in a basis set of $n_b = 300$ B splines of order $k = 8$ in a finite region (here $R = 0$ to 15 a.u.).

The integral $\int d\varepsilon_\alpha$ in Eq. (4) was performed in an energy-grid quadrature consisting of 45 points evenly spaced in momentum k ($\varepsilon = k^2/2$) with spacing $\Delta k = \pi/240$. The scattering states $\psi_{\alpha l_\alpha m_\alpha}^{\varepsilon_\alpha(-)}(\mathbf{r};R)$ were calculated at each internuclear distance using a multichannel configuration-interaction (MCCI) method [7–9,29,43]. The MCCI N-electron wave function for a given electron energy was represented in a single-center expanded grid, with a partial wave expansion up to $l_{max} = 40$. A CAS configuration-interaction calculation was used to compute the ion target states that define the channels of the close-coupling calculation. The lowest five ion states were included in the close-coupling expansion: $1\,^2\Sigma^+$ (energetically open, appearing in Fig. 1) at 7.99 eV, $2\,^2\Sigma^+$ at 19.94 eV, $1\,^2\Pi$ (both components) at 20.78 eV, and $3\,^2\Sigma^+$ at 23.71 eV closed channels. The $^2\Sigma^+$ states have 424 CSFs, and the $^2\Pi$ states have 340 CSFs. Further increasing the number of channels in the close-coupling expansion did not significantly change the results.

III. RESULTS OF PUMP AND IONIZING PROBE CALCULATIONS

A. Photoelectron energies and dissociation energies

We consider a two-pulse scheme consisting of a 200-nm ($\hbar\omega = 6.20\,\text{eV}$) pulse in combination with a 266-nm ($\hbar\omega = 4.66\,\text{eV}$) pulse, both of intensity $I = 10^{12}$ W cm^{-2} and temporal duration $T = 5$ fs with a $\sin^2(\pi t/T)$ envelope. Depending on the order of the pulses either can serve as a pump or ionizing probe. Both pulses are linearly polarized, and their corresponding polarization vectors are chosen to be perpendicular to the molecular axis. The time delay between the pulses Δt has been defined as the difference between the times at which they reach the maximum amplitude. Negative time delays imply that the 266-nm pulse arrives before the 200-nm one. The central energy of the pulses is such that a two-photon absorption, from either pulse or one from each, is needed in order to ionize the molecule. Due to dipole selection rules, one absorbed photon from the $X\,^1\Sigma^+$ ground state leads to states of $^1\Pi$ symmetry, while two absorbed photons lead to states of $^1\Sigma^+$ and $^1\Delta$ final symmetries. One-photon absorption from the 266-nm pulse leads mainly to excitation of the $2p\pi$ state centered at a photon energy of 4.5 eV, while one-photon absorption from the 200-nm pulse leads mainly to excitation of the $3p\pi$ and $3d\pi$ states centered at 6.39 eV. These peak absorptions are due to the pulses' bandwidths in combination with the Franck-Condon factors between the ground and excited states.

Figure 2(a) shows the electron-kinetic-energy (EKE) spectrum obtained in these calculations as a function of the pump-probe delay integrated over the nuclear kinetic-energy release of the ionic dissociation continuum and summed over the few bound vibrational states of LiH$^+$. The spectrum exhibits three distinct features as a function of the delay, each
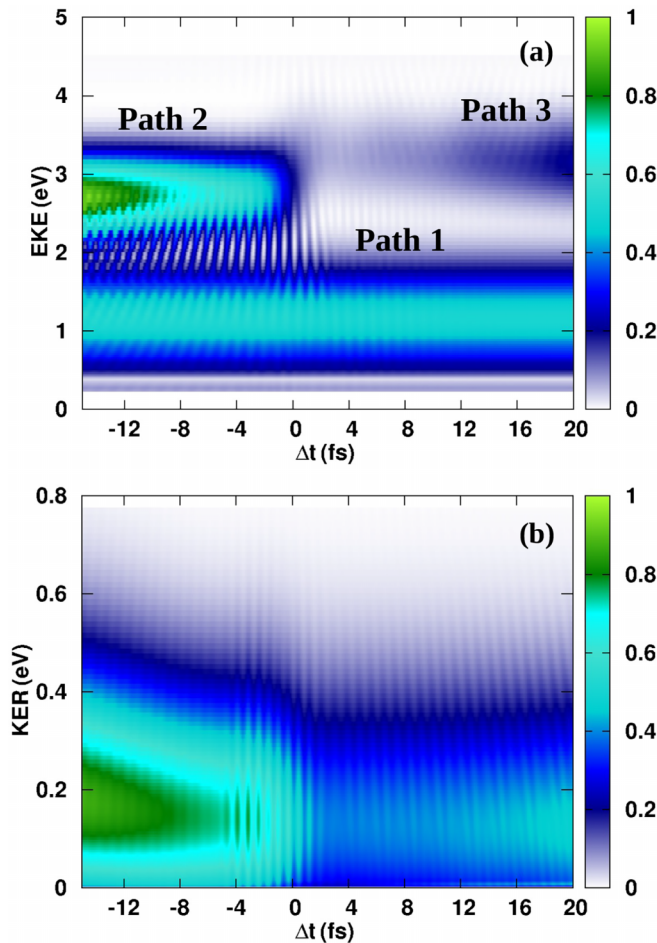
FIG. 2. Ionization probability distributions as a function of the time delay of the 5-fs 266-nm pulse relative to the 5-fs 200-nm pulse. Negative time delays mean that the 266-nm pulse arrives first. (a) Probability distribution of electron kinetic energy, integrated over nuclear kinetic-energy release (KER) in the dissociation of $Li^+ + H$ and summed over bound vibrational states of LiH^+. (b) Probability distribution of KER integrated over photoelectron kinetic energy.

representing a different ionization path. The first feature, centered at 1.2 eV in Fig. 2(a) and appearing at all time delays, results from 266-nm one-color, two-photon resonant ionization through the $B^1\Pi(2p\pi)$ excited state. Taking into account the potential for dissociative ionization ($= 7.79$ eV), energy conservation leads, indeed, to an electron-kinetic-energy spectrum centered around $4.5\,\text{eV} + 4.5\,\text{eV} - 7.79\,\text{eV} = 1.21\,\text{eV}$. That pathway to ionization is denoted "Path 1" in Fig. 2(a) and is depicted in Fig. 1(a). The second pathway to ionization, centered at an EKE of 2.7 eV and appearing only at negative delays, results from two-color, two-photon resonant ionization through the $B^1\Pi(2p\pi)$ excited state involving one 266-nm photon and a second 200-nm photon. Energy conservation leads, indeed, to an electron-kinetic-energy spectrum centered around $4.5\,\text{eV} + 6.2\,\text{eV} - 7.79\,\text{eV} = 2.91\,\text{eV}$. That process is labeled "Path 2" in Fig. 2(a) and is depicted in Fig. 1(b). At these negative delays the 266-nm pulse creates a wave packet in the $B^1\Pi(2p\pi)$ excited state which is then ionized after some delay by the 200-nm pulse. A third and weaker feature in Fig. 2(a) is centered at an EKE

of 3.2 eV and appears at large positive delays. As in the previous case, this feature results from a two-color resonant ionization, but this time through the $3p\pi$, $3d\pi$, and (to a lesser extent) $4p\pi$ $^1\Pi$ Rydberg states. Energy conservation leads, indeed, to an electron-kinetic-energy spectrum centered around $4.66\,\text{eV} + 6.39\,\text{eV} - 7.79\,\text{eV} = 3.26\,\text{eV}$. At these delays the 200-nm pulse creates a wave packet in these Rydberg states which is then, after some delay, ionized by the 266-nm pulse, and this pathway to dissociative ionization is labeled "Path 3" in Fig. 2(a) and is depicted in Fig. 1(c). The 5-fs $\sin^2$ pulses used in these simulations have an energy bandwidth with full width at half maximum (FWHM) of about 1.24 eV, and the relative intensities of these ionization pathways of course depend on the pulse duration.

The lower intensity of the third feature compared to the first and second ones is a direct consequence of small dipole couplings connecting the ground state of the molecule with those Rydberg states. The magnitude of these dipole couplings decreases higher in the Rydberg series, scaling as $(n - \delta)^{-3/2}$, where n and δ are the principal quantum number and the quantum defect of the Rydberg states, respectively [38].

The third feature in Fig. 2(a) also becomes noticeably more intense with longer delays. That behavior is a consequence of the fact that the dissociative nuclear dynamics on the higher Rydberg states is being observed through the photoionization of the moving wave packet, and the photoionization process, the lens through which we view the dynamics, itself depends on geometry. For short delays the dissociating wave packet on the $3p\pi$ state in particular is in a local minimum in the photoionization cross section, and only for longer delays does it reach regions where it is more effectively probed by the 266-nm pulse. The origin of this effect can be observed in Fig. 3, where the dependence of the relevant photoionization cross sections on internuclear distance is shown. The total photoionization cross section is depicted for one-photon absorption from the $2p\pi$, $3p\pi$, $3d\pi$, and $4p\pi$ excited states, leading to the ionization continuum of $^1\Sigma^+$ (top three panels) and $^1\Delta$ (bottom three panels) symmetries.

A fourth possible path consists of a one-color, two-photon absorption at 200 nm. This path was, nevertheless, found to be negligibly weak in these calculations. The weakness of this two-photon absorption is due to the low probabilities for excitation of the $3p\pi$, $3d\pi$, and $4p\pi$ states from the ground state, as seen in path 3, in combination with rapidly decreasing ionization amplitudes with increasing photon energy.

In addition, the EKE spectrum in Fig. 2(a) presents interference fringes at negative delays. These fringes are a consequence of the overlap in energy of the 200- and 266-nm pulses which have bandwidths (FWHM $\approx 3\pi/T$) of 1.24 eV. The 266-nm probe pulse creates a superposition of the initial vibrational state and the vibrational (dissociative) states of the $B^1\Pi(2p\pi)$ intermediate state, with an energy difference of around 5 eV. The superpositions of those states with the ground vibrational state have beat frequencies with periods ($\tau = 2\pi\hbar/\Delta E$) around 0.82 fs. Thus, depending on the phases of those oscillations when it encounters them, the 200-nm pulse can either stimulate emission back to the ground state, further increase the population in the intermediate state, or ionize from the intermediate state. The net result is that the ionized signal oscillates as a function of the time delay with a
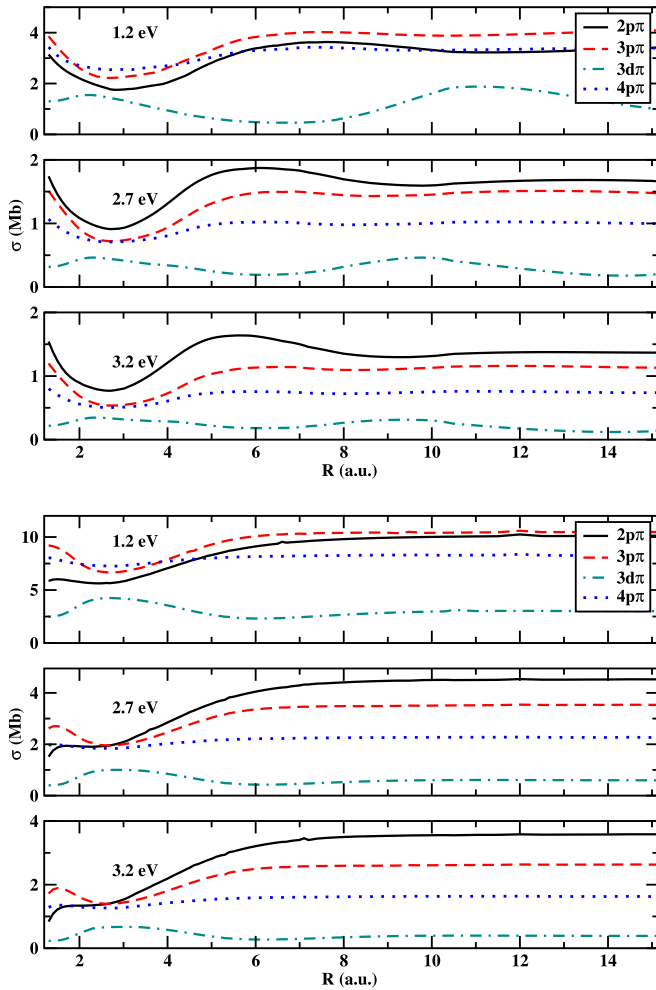
FIG. 3. The top three panels show the integral photoionization cross sections as a function of internuclear distance for ionization into the ionization continuum of $^1\Sigma^+$ symmetry. The bottom three panels show the integral photoionization cross sections for ionization into the $^1\Delta$ continuum. The complex amplitudes determining the couplings between electronic states used in calculations here (see, e.g., Eq. (19) of Ref. [29]) are summed and squared to yield these cross sections.

period near a femtosecond. A similar effect was previously observed when identical durations and central frequencies were used for both the pump and probe pulses [20,29].

Figure 2(b) shows the kinetic-energy release (KER; continuum energy of the $Li^+ + H$ dissociation) integrated over the photoelectron energy and angular distribution. The KER spectrum exhibits the interference fringes discussed above. In contrast to the EKE spectrum, the different one-color and two-color ionization paths cannot be distinguished in the KER time-delay spectrum. At negative time delays, where path 1 and path 2 contribute, the KER becomes narrower, with the peak shifting to slightly lower KER as the time delay approaches zero. Whereas at positive time delay, in which path 1 and path 3 contribute, there is very little change in the width and position of the KER with increasing time delay, there is an increase in the intensity as path 3 becomes stronger at longer time delays.

Coincidence measurements of the nuclear kinetic-energy release and photoelectron energy can cleanly separate the contributions from each path in the KER distributions shown in Fig. 2(b). The joint distribution for negative time delays is shown in the left column of Fig. 4. The signal from path 1 remains static in the left of those images at lower EKE (on the left in each panel) because this one-color, 266-nm, two-photon path does not depend on the arrival time of the 200-nm pulse, as indicated in Fig. 1.

Gim and Lee [38] pointed out that while the higher Rydberg states closely parallel the parent $X\,^2\Sigma^+$ state of LiH^+, the $B\,^1\Pi(2p\pi)$ state deviates from that behavior somewhat. That difference in the shapes of the potentials for the Rydberg states has consequences for the processes we study here that can be seen by comparing the results of coincidence measurements for positive and negative delays of the 266-nm pulse relative to the 200-nm pulse.

The signal from path 2 at higher EKE, visible at higher EKE in the left column of Fig. 4, shows that at large negative delays the wave packet on the $B\,^1\Pi(2p\pi)$ state has a somewhat higher KER than when the time delays are closer to zero, with the peak in the KER shifting from 0.2 eV at a time delay of -15 fs to 0.1 eV at 0 fs. This behavior can be understood by considering the difference in the PECs of the $B\,^1\Pi(2p\pi)$ state of LiH, with a well depth of 0.036 eV, and the $X\,^2\Sigma^+$ state of LiH^+, with a well depth 0.142 eV [38]. In this case, with a short time between the pulses, the system will be excited to the ion near its minimum, so the nuclei will require the full 0.142 eV to break the Li-H bond on the ion state PEC, leading to a lower KER. In contrast, when there is a long time between the pulses, the bond will be broken in the lower state before the system is ionized, thus requiring only 0.036 eV to break the bond, leading to a higher KER. This analysis agrees nicely with the 0.1-eV shift in the KER peaks.

For positive time delays, shown in the right column of Fig. 4, path 2 is extinguished, and the dynamics of path 3 appear. Again, the signal from path 1 remains static, depending only on a single pulse. The dynamics of the wave packets dissociating (primarily) on the nearly parallel $3p\pi$ and $3d\pi$ states are now visible at larger EKE (on the right in each panel). For these intermediate states, the well depths of the PECs of the Rydberg states are almost identical to each other's well depths of 0.142 eV for $3p\pi$ and 0.125 eV for $3d\pi$ and to the ion state with a well depth of 0.142 eV [38]. Thus, both KER and EKE will be nearly constant with time delay due to the nearly parallel PECs for the Rydberg neutral states and the ground state of LiH^+.

B. Photoelectron angular dependence in the body frame

In earlier calculations of pump-probe dissociative ionization through the $A\,^1\Sigma^+$ lowest valence excited state of LiH [29], the molecular-frame photoelectron angular distributions (MFPADs) directly reflected nuclear dynamics on the intermediate state via the change in its character from ionic to valence and the resulting change in the MFPAD. Here we probe the dynamics of intermediate Rydberg states, and the situation is different. In Fig. 5 we show the MFPADs integrated over KER for three different photoelectron energies, 1.23, 1.96, and 2.69 eV, for the same $\Delta t = -4$ fs delay. These
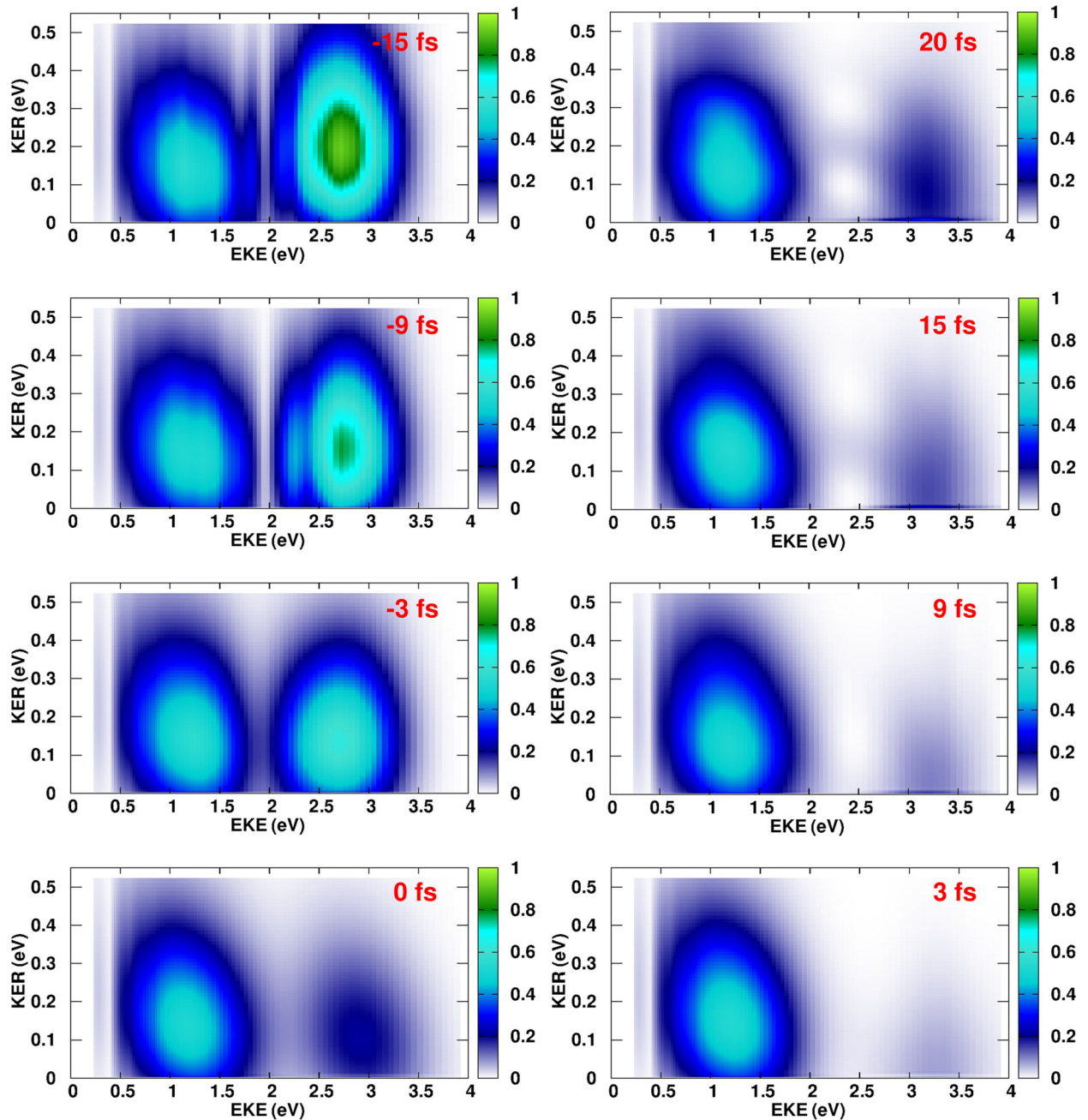
FIG. 4. Left column: joint distribution of nuclear kinetic-energy release and photoelectron kinetic energy for dissociative ionization at negative delays of, from top to bottom, -15, -9, -3, and 0 fs. Right column: joint distribution of nuclear kinetic-energy release and photoelectron kinetic energy for dissociative ionization at positive delays of, from top to bottom, 20, 15, 9, and 3 fs.

energies were chosen to match the center of the distributions correlated to each ionization path and a point energetically between them [see Fig. 2(a)]. For the lowest photoelectron energy [Fig. 5(a)], the MFPAD features a prominent lobe towards the H atom exhibiting nearly equal photoelectron flux parallel and perpendicular to the molecular axis, even though the light polarization vector is perpendicular to it. At these photoelectron energies the photoionization process is dominated by the $\varepsilon d(^1\Delta)$ and $\varepsilon s(^1\Sigma^+)$ channels. For higher photoelectron energies, the photoelectron flux perpendicular to the molecular axis decreases while, simultaneously, the parallel flux increases mainly towards the Li atom. The observed

change in the shapes of the MFPADs with energy reflects the diminishing photoionization partial cross sections leading to the $^1\Delta$ symmetry with respect to the one leading to the $^1\Sigma^+$ symmetry as the photoelectron energy increases from that of path 1 to that of path 2 (see Fig. 3). The ratio between the two dominant channels indeed decreases considerably from $R = \varepsilon d(^1\Delta)/\varepsilon s(^1\Sigma^+) \sim 7$ at 1.2 eV to $R \sim 3$ at 3.2 eV.

Figure 6 shows the MFPADs, integrated over KER, for photoelectron energies with EKE of 2.69 eV at $\Delta t = -6$ fs and EKE of 3.20 eV at $\Delta t = 12$ fs. The former corresponds to the two-color, two-photon resonant ionization through the $2p\pi$ excited state (path 1), as in Fig. 5(c), but at a different
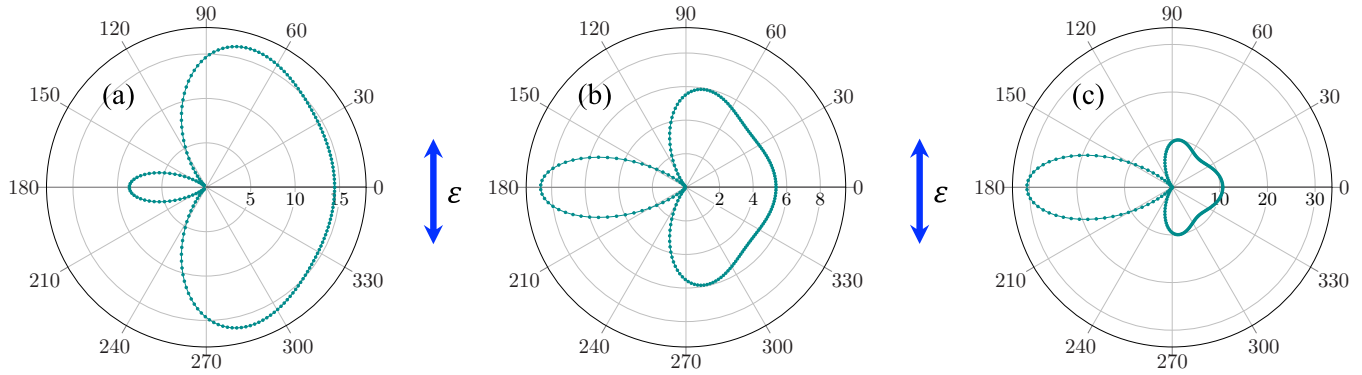
FIG. 5. MFPADs at $\Delta t = -4$ fs of delay between the 266- and 200-nm pulses for different energies of the photoelectron and integrated over the kinetic-energy release. (a) EKE is 1.23 eV, (b) EKE is 1.96 eV, and (c) EKE is 2.69 eV (arbitrary units but the same scale). The molecule is placed perpendicular to the light polarization vector (blue double-ended arrow), with the Li atom on the left.

delay, while the latter is associated with the two-color resonant ionization through the $3p\pi$, $3d\pi$, and $4p\pi$ Rydberg states (path 3). In contrast to our earlier study [29], in which the variations in the MFPADs with the delay were used to map the nuclear wave-packet movements in the PEC of a bound electronic state, here the MFPADs exhibit almost no change with the delay. In the present calculations the significant changes in the MFPADs occur with varying photoelectron energy rather than the delay between the pump and the probe.

IV. CONCLUSION

The calculations presented here for pump-probe dynamics on the π Rydberg states of LiH provide a model for such experiments on Rydberg states of other diatomics. The electron kinetic energy and nuclear kinetic-energy release, taken together, reveal the multiple-pathway dissociative ionization that will exist in general because the photon energy of a pulse that can excite Rydberg states will frequently be able to ionize it as well. However, as these calculations demonstrate, coincidence measurements of those two quantities will generally be necessary to reveal wave-packet motion on the intermediate dissociative Rydberg states as a function of time delay. Our results also suggest that those coincidence measurements also have the potential to reveal subtle differences between the dynamics associated with lower and higher Rydberg states. In contrast to other cases [29] in which the intermediate electronic state or final ionic state changes character with geometry, the angular distributions of the photoelectrons in the body frame are almost constant in shape for all delays. Instead, differences in MFPADs for different pathways primarily reflect changes in the photoionization amplitudes with energy.

The calculations presented here further establish the applicability of this approach to treat simultaneously nuclear dynamics and the correlated electronic dynamics of photoionization. Accurate determination of photoionization amplitudes over a range of internuclear distances in multichannel

calculations is now nearly routine using the Schwinger variational method [44,45], at least for linear molecules. Therefore, it can be expected that applications of the formalism we use here to other diatomics promise to guide and enhance the picture of intermediate-state dynamics that pump-probe experiments can provide.
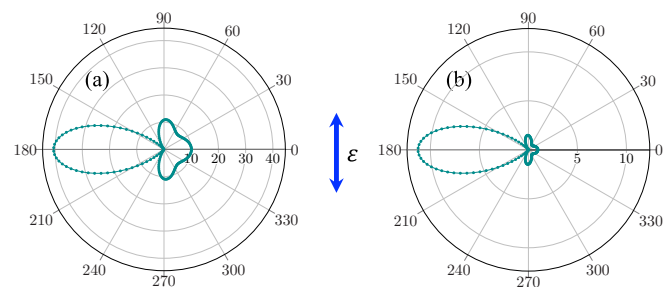
FIG. 6. As in Fig. 5 for different photoelectron energies at different delays between the 266- and 200-nm pulses. (a) EKE is 2.69 eV at $\Delta t = -6$ fs, and (b) EKE is 3.20 eV at $\Delta t = 12$ fs. The molecule is placed perpendicular to the light polarization vector (blue double-ended arrow), with the Li atom on the left.

[1] R. R. Lucchese, G. Raseev, and V. McKoy, Studies of differential and total photoionization cross sections of molecular nitrogen, Phys. Rev. A **25**, 2572 (1982).

[2] T. N. Rescigno, B. H. Lengsfield III, and A. E. Orel, Interchannel coupling and ground state correlation effects in the photoionization of CO, J. Chem. Phys. **99**, 5097 (1993).

[3] T. N. Rescigno, C. W. McCurdy, A. E. Orel, and B. H. Lengsfield III, The complex kohn variational method, *Computational Methods for Electron-Molecule Collisions* (Springer, New York, 1995), pp. 1–44.

[4] T. N. Rescigno, B. H. Lengsfield III, and C. W. McCurdy, The incorporation of modern electronic structure methods in electron-molecule collision problems: Variational calculations using the complex Kohn method, in *Modern Electronic Structure Theory*, edited by D. R. Yarkony (World Scientific, Singapore, 1995), Vol. 1, pp. 501–588.

[5] R. R. Lucchese, K. Takatsuka, and V. McKoy, Applications of the Schwinger variational principle to electron-molecule collisions and molecular photoionization, Phys. Rep. **131**, 147 (1986).

[6] B. Basden and R. R. Lucchese, Angular distributions of $N_2(2\sigma_u)^{-1}$ photoelectrons including the effects of coupling to the $N_2(3\sigma_g)^{-1}$ channel, Phys. Rev. A **34**, 5158 (1986).

[7] R. E. Stratmann and R. R. Lucchese, A graphical unitary group approach to study multiplet specific multichannel electron correlation effects in the photoionization of O_2, J. Chem. Phys. **102**, 8493 (1995).

[8] R. E. Stratmann, R. W. Zurales, and R. R. Lucchese, Multiplet-specific multichannel electron-correlation effects in the photoionization of NO, J. Chem. Phys. **104**, 8989 (1996).

[9] R. R. Lucchese, Effects of interchannel coupling on the photoionization cross sections of carbon dioxide, J. Chem. Phys. **92**, 4203 (1990).

[10] L. Greenman, R. R. Lucchese, and C. W. McCurdy, Variational treatment of electron–polyatomic-molecule scattering calculations using adaptive overset grids, Phys. Rev. A **96**, 052706 (2017).

[11] C. A. Marante, L. Greenman, C. S. Trevisan, T. N. Rescigno, C. W. McCurdy, and R. R. Lucchese, Validity of the static-exchange approximation for inner-shell photoionization of polyatomic molecules, Phys. Rev. A **102**, 012815 (2020).

[12] D. Toffoli and P. Decleva, A multichannel least-squares B-spline approach to molecular photoionization: Theory, implementation, and applications within the configuration–interaction singles approximation, J. Chem. Theory Comput. **12**, 4996 (2016).

[13] J. D. Gorfinkiel and J. Tennyson, Electron impact ionization of small molecules at intermediate energies: The molecular R-matrix with pseudostates method, J. Phys. B **38**, 1607 (2005).

[14] S. M. Poullain, M. Klinker, J. González-Vázquez, and F. Martín, Resonant photoionization of O_2 up to the fourth ionization threshold, Phys. Chem. Chem. Phys. **21**, 16497 (2019).

[15] A. Palacios, J. L. Sanz-Vicario, and F. Martín, Theoretical methods for attosecond electron and nuclear dynamics: Applications to the H_2 molecule, J. Phys. B **48**, 242001 (2015).

[16] J. L. Sanz-Vicario, H. Bachau, and F. Martín, Time-dependent theoretical description of molecular autoionization produced by femtosecond XUV laser pulses, Phys. Rev. A **73**, 033410 (2006).

[17] R. Y. Bello, S. E. Canton, D. Jelovina, J. D. Bozek, B. Rude, O. Smirnova, M. Y. Ivanov, A. Palacios, and F. Martín, Reconstruction of the time-dependent electronic wave packet arising from molecular autoionization, Sci. Adv. **4**, eaat3962 (2018).

[18] A. Palacios and F. Martín, The quantum chemistry of attosecond molecular science, Wiley Interdiscip. Rev.: Comput. Mol. Sci. **10**, e1430 (2020).

[19] R. Y. Bello, F. Martín, and A. Palacios, Attosecond laser control of photoelectron angular distributions in XUV-induced ionization of H_2, Faraday Discuss. **228**, 378 (2021).

[20] A. Palacios, A. González-Castrillo, and F. Martín, Molecular interferometer to decode attosecond electron–nuclear dynamics, Proc. Natl. Acad. Sci. USA **111**, 3973 (2014).

[21] R. Y. Bello, V. J. Borràs, J. González-Vázquez, and F. Martín, Electronic coherences in argon through interfering one- and two-photon ionization processes in the vicinity of Feshbach resonances, Phys. Rev. Res. **4**, 043028 (2022).

[22] Y. Arasaki, K. Takatsuka, K. Wang, and V. McKoy, Studies of electron transfer in NaI with pump-probe femtosecond photoelectron spectroscopy, J. Chem. Phys. **119**, 7913 (2003).

[23] Y. Arasaki, K. Takatsuka, K. Wand, and V. McKoy, Time-resolved photoelectron spectroscopy of wavepackets through a conical intersection in NO_2, J. Chem. Phys **132**, 124307 (2010).

[24] Y. Arasaki, K. Wang, V. McKoy, and K. Takatsuka, Monitoring the effect of a control pulse on a conical intersection by time-resolved photoelectron spectroscopy, Phys. Chem. Chem. Phys. **13**, 8681 (2011).

[25] Y. Arasaki, K. Wang, V. McKoy, and K. Takatsuka, Nuclear and electron dynamics from femto- and subfemto-second time-resolved photoelectron angular distributions, J. Phys. B **45**, 194006 (2012).

[26] A. von Conta, A. Tehlar, A. Schletter, Y. Arasaki, K. Takatsuka, and H. J. Wörner, Conical-intersection dynamics and ground-state chemistry probed by extreme-ultraviolet time-resolved photoelectron spectroscopy, Nat. Commun. **9**, 3162 (2018).

[27] S. Nandi, E. Plésiat, S. Zhong, A. Palacios, D. Busto, M. Isinger, L. Neoričić, C. L. Arnold, R. J. Squibb, R. Feifel, P. Decleva, A. L'Huillier, F. Martín, and M. Gisselbrecht, Attosecond timing of electron emission from a molecular shape resonance, Sci. Adv. **6**, eaba7762 (2020).

[28] R. R. Lucchese and V. McKoy, Iterative approach to the Schwinger variational principle applied to electron-molecular-ion collisions, Phys. Rev. A **24**, 770 (1981).

[29] R. Y. Bello, R. R. Lucchese, T. N. Rescigno, and C. W. McCurdy, Correlated variational treatment of ionization coupled to nuclear motion: Ultrafast pump and ionizing probe of electronic and nuclear dynamics in LiH, Phys. Rev. Res. **3**, 013228 (2021).

[30] F. Remacle and R. D. Levine, Attosecond pumping of nonstationary electronic states of LiH: Charge shake-up and electron density distortion, Phys. Rev. A **83**, 013411 (2011).

[31] B. Mignolet, R. D. Levine, and F. Remacle, Control of electronic dynamics visualized by angularly resolved photoelectron spectra: A dynamical simulation with an IR pump and XUV attosecond-pulse-train probe, Phys. Rev. A **89**, 021403(R) (2014).

[32] A. Nikodem, R. D. Levine, and F. Remacle, Quantum nuclear dynamics pumped and probed by ultrafast polarization controlled steering of a coherent electronic state in LiH, J. Phys. Chem. A **120**, 3343 (2016).

[33] A. Nikodem, R. D. Levine, and F. Remacle, Spatial and temporal control of populations, branching ratios, and electronic coherences in LiH by a single one-cycle infrared pulse, Phys. Rev. A **95**, 053404 (2017).

[34] S. van den Wildenberg, B. Mignolet, R. D. Levine, and F. Remacle, Temporal and spatially resolved imaging of the correlated nuclear-electronic dynamics and of the ionized photoelectron in a coherently electronically highly excited vibrating LiH molecule, J. Chem. Phys. **151**, 134310 (2019).

[35] F. X. Gadéa and T. Leininger, Accurate ab initio calculations for LiH and its ions, LiH^+ and LiH^-, Theor. Chem. Acc. **116**, 566 (2006).

[36] A. Boutalib and F. X. Gadéa, Ab initio adiabatic and diabatic potential energy curves of the LiH molecule, J. Chem. Phys. **97**, 1144 (1992).

[37] H. Berriche and F. X. Gadéa, Ab initio adiabatic and diabatic permanent dipoles for the low-lying states of the LiH molecule. A direct illustration of the ionic character, Chem. Phys. Lett. **247**, 85 (1995).

[38] Y. Gim and C.-W. Lee, Studies of singlet Rydberg series of LiH derived from Li(nl) + H(1s), with $n \leqslant 6$ and $l \leqslant 4$, J. Chem. Phys. **141**, 144313 (2014).

[39] H.-J. Kim, C.-W. Lee, and Y.-J. Cheong, Transition of the Rydberg series from the spectroscopic to the united atom region in LiH, J. Phys. B **49**, 235101 (2016).

[40] H.-J. Werner, P. J. Knowles, G. Knizia, F. R. Manby, and M. Schütz, Molpro: A general-purpose quantum chemistry program package, Wiley Interdiscip. Rev.: Comput. Mol. Sci. **2**, 242 (2012).

[41] H.-J. Werner *et al.*, MOLPRO, a package of *ab initio* programs, version 2015.1, http://www.molpro.net.

[42] K. Kaufmann, W. Baumeister, and M. Jungen, Universal Gaussian basis sets for an optimum representation of Rydberg and continuum wavefunctions, J. Phys. B **22**, 2223 (1989).

[43] P. Lin and R. R. Lucchese, Theoretical studies of cross sections and photoelectron angular distributions in the valence photoionization of molecular oxygen, J. Chem. Phys. **116**, 8863 (2002).

[44] Y.-C. Lin, A. P. Fidler, A. Sandhu, R. R. Lucchese, C. W. McCurdy, S. R. Leone, and D. M. Neumark, Coupled nuclear–electronic decay dynamics of O_2 inner valence excited states revealed by attosecond XUV wave-mixing spectroscopy, Faraday Discuss. **228**, 537 (2021).

[45] A. P. Fidler, Y.-C. Lin, J. D. Gaynor, C. W. McCurdy, S. R. Leone, R. R. Lucchese, and D. M. Neumark, State-selective probing of CO_2 autoionizing inner valence Rydberg states with attosecond extreme ultraviolet four-wave-mixing spectroscopy, Phys. Rev. A **106**, 063525 (2022).